

Copyright © 1992, by the author(s).
All rights reserved.

Permission to make digital or hard copies of all or part of this work for personal or classroom use is granted without fee provided that copies are not made or distributed for profit or commercial advantage and that copies bear this notice and the full citation on the first page. To copy otherwise, to republish, to post on servers or to redistribute to lists, requires prior specific permission.

**TWO-DIMENSIONAL ELECTROMAGNETIC
SIMULATION OF TOPOGRAPHY SCATTERING AND
DIFFRACTION FOR OPTICAL LITHOGRAPHY**

by

Alfred K. Wong

Memorandum No. UCB/ERL M92/115

12 October 1992

**TWO-DIMENSIONAL ELECTROMAGNETIC
SIMULATION OF TOPOGRAPHY SCATTERING AND
DIFFRACTION FOR OPTICAL LITHOGRAPHY**

by

Alfred K. Wong

Memorandum No. UCB/ERL M92/115

12 October 1992

ELECTRONICS RESEARCH LABORATORY

College of Engineering
University of California, Berkeley
94720

TITLE PAGE

**TWO-DIMENSIONAL ELECTROMAGNETIC
SIMULATION OF TOPOGRAPHY SCATTERING AND
DIFFRACTION FOR OPTICAL LITHOGRAPHY**

by

Alfred K. Wong

Memorandum No. UCB/ERL M92/115

12 October 1992

ELECTRONICS RESEARCH LABORATORY

College of Engineering
University of California, Berkeley
94720

Two-dimensional Electromagnetic Simulation of Topography Scattering and Diffraction for Optical Lithography

Alfred K. Wong

Department of Electrical Engineering and Computer Sciences

University of California, Berkeley

October 12, 1992.

Abstract

The time-domain finite-difference approach used by TEMPEST for electromagnetic scattering and diffraction simulation has been extended from the transverse electric (TE) polarization to the transverse magnetic (TM) polarization. The equations for the TM polarization have the same form as those of the TE polarization. Hence, simulation efficiencies (per iteration) of both polarizations are similar. Extension to off-axis incident analysis has also been made. Implementation of oblique incidence has included a synchronization between the analytically calculated sinusoidal forcing function and the propagated wave. With these two additional computing capabilities, a new version of the simulation program TEMPEST written in the programming language C* is available. This version is easier to use than the previous *lisp version. The improved program has been applied to the studying of polarization effects in mask transmission for different mask technologies. Future extensions of the program, to include three-dimensional and partial coherence effects, as well as analysis of propagation in highly dispersive materials, are also discussed.

Acknowledgments

I would like to thank my advisor, Professor Andrew Neureuther, for his encouragement and patient guidance throughout this project. Professor Mei and Professor Oldham had also given me valuable insight into problems concerning electromagnetic simulation and photolithography. The assistance of my colleagues who had previously been involved in the project was essential for my understanding of the problem. John Gamelin, Dr. Roberto Guerrieri of the Universita' di Bologna, Italy, and Karim Tadros had all made constructive suggestions and critical discussions which led to the final result of the simulation program TEMPEST version 2.0.

The friendly and warm working atmosphere within the research group had fostered meaningful discussions and novel ideas which were indispensable to the success of this project. I am grateful to Michael Yeung for numerous discussions on electromagnetic scattering simulation methods. His vast knowledge in this field and his approach to the problem had a strong influence on me. I would also like to thank Richard Ferguson, Bill Partlo, and Kenny Toh for insightful discussions and help.

This research was supported by the Charles LeGeyt Fortescue Fellowship, an IBM Fellowship, and the SRC/SEMATECH contract #91-MC-500.

Table of Contents

Chapter 1:	Introduction	1
Chapter 2:	Transverse Magnetic (TM) Polarization	4
2.1	Statement of the Problem	4
2.2	Solution for the TE Polarization	5
2.3	Extension to the TM Polarization	6
2.4	Implementation	7
Chapter 3:	Oblique Incidence	9
3.1	Introduction	9
3.2	Left-right Periodic Boundary Condition	9
3.3	Domain Excitation	11
3.4	Dispersion Relation	12
Chapter 4:	Image Synthesis	13
4.1	Motivation	13
4.2	Formulation	13
4.3	Validity of the Assumptions	15
Chapter 5:	Current Status of TEMPEST	18
Chapter 6:	Applications to Mask Transmission	20
6.1	Abstract	20
6.2	Introduction	21
6.3	Simulation Techniques	21
6.4	Chrome Edge Effects	22
6.5	Mask Overcoating Effects	26
6.6	Phase-shifting Material Edge Effects	29
6.7	Reflective Masks	32
6.8	Conclusion	34
Chapter 7:	Conclusions and Future Work	35
References		37

Chapter 1

Introduction

With the introduction of new technologies and with the scaling of optical lithography, computer simulation of electromagnetic scattering from wafer topography and diffraction through apertures in masks is increasingly important. To accurately predict subtle effects such as those of edge shape on masks and small changes in alignment mark geometry requires rigorous numerical models of wave propagation. On the other hand, such a rigorous approach must be efficient in order to provide a solution quickly and must also be convenient to use.

TEMPEST¹ solves Maxwell's equations using the time-domain finite-difference approach proposed by Yee² and extended by Wojcik³. The algorithm is implemented on a single instruction multiple data computer architecture called the connection machine (CM) where the electric field and magnetic field are staggered over a two-dimensional uniformly spaced grid. Electromagnetic wave propagation and scattering are simulated by solving iteratively the discretized Maxwell's equations until the electromagnetic field inside the simulation domain reaches steady-state.

Although the previous version of TEMPEST was limited to analyzing problems with normally incident transverse electric (TE) illumination, the program had been useful in areas of photolithography⁴, optical metrology⁵, signal integrity in mask transmission⁶, and alignment mark signal quality⁷. In this report, extensions of the previous algorithm to the transverse magnetic (TM) polarization as well as oblique incidence are discussed. The extended version of the simulation program does not only have added capabilities, but is also simple to use via telnet or remote login to a CM front-end machine.

The symmetries and asymmetries between the TE and TM polarizations are discussed in Chapter 2. With the substitutions $E \rightarrow H$, $H \rightarrow E$, $\epsilon \rightarrow -\mu$, and $\mu \rightarrow -\epsilon$, most of the equations for the TE polarization can be used for the TM polarization. The exceptions are equations which are functions of the electric conductivity. Extension of the

algorithm to solve obliquely incident problems is discussed in Chapter 3. The assumption of periodic structures together with the left-right periodic boundary condition greatly simplify the problem. However, the simulation domain must be excited in such a way that the analytically calculated excitation function and the numerically waves are properly synchronized.

In Chapter 4, optical image synthesis from the diffraction harmonics generated by TEMPEST is discussed. Although TEMPEST assumes coherent illumination, partial coherent effects can be approximated by the assumption of constant diffraction efficiencies with respect to illumination angle. This approximation is reasonable provided that the incident angle is less than 40° , i.e., the numerical aperture (NA) of the optical system is less than 0.65. The extension of TEMPEST for oblique incidence analysis has allowed this assumption to be tested.

Chapter 5 gives a brief description of the current status of the program. The code has been re-written from the *lisp programming language to the C* language. As a result, TEMPEST has become more convenient to use and more user friendly. Any person who obtains an account on any front-end machine to a CM can run TEMPEST via telnet or remote login. Execution of the program no longer requires loading of object codes and issuing of a complicated sequence of commands.

Applications of TEMPEST in mask transmission studies are discussed in Chapter 6. Four mask technologies are assessed: chrome mask, overcoated mask, chromeless phase-shift mask, and reflective mask. TEMPEST simulation shows that polarization effects are important for 1X chrome masks, material effects are important in overcoated and reflective masks, but edge effects are not important for reduction chromeless phase-shift masks. For alternating phase-shift masks, however, degradation of the optical signal due to interaction between the metal edge and the etched glass edge can be significant.

Chapter 7 presents some possible extensions to the current simulation program. Extension of TEMPEST to solve three-dimensional problems may need new techniques or bigger CM with more nodes than those that are currently available.

Chapter 2

Transverse Magnetic (TM) Polarization

2.1 Statement of the Problem

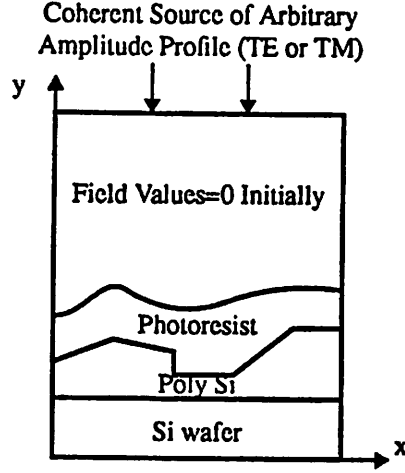


Figure 2.1 A typical simulation domain in TEMPEST. The domain is excited at the top by a monochromatic and coherent plane wave.

A typical simulation domain in TEMPEST is shown in Figure 2.1. The structure can represent arbitrary two-dimensional non-planar and inhomogeneous topography. The simulation domain is excited with monochromatic radiation at the top. The problem is to find the steady-state solution for the following set of equations:

$$\nabla \times \vec{H} = \frac{\partial \vec{D}}{\partial t} + \vec{J} \quad (2.1)$$

$$\nabla \times \vec{E} = -\frac{\partial \vec{B}}{\partial t} \quad (2.2)$$

supplemented with the relations:

$$\vec{B} = \mu \vec{H} \quad (2.3)$$

$$\vec{D} = \epsilon \vec{E} \quad (2.4)$$

$$\vec{J} = \sigma \vec{E} \quad (2.5)$$

where μ , ϵ , and σ are the permittivity, permeability, and conductivity of the material, respectively.

2.2 Solution for the TE Polarization

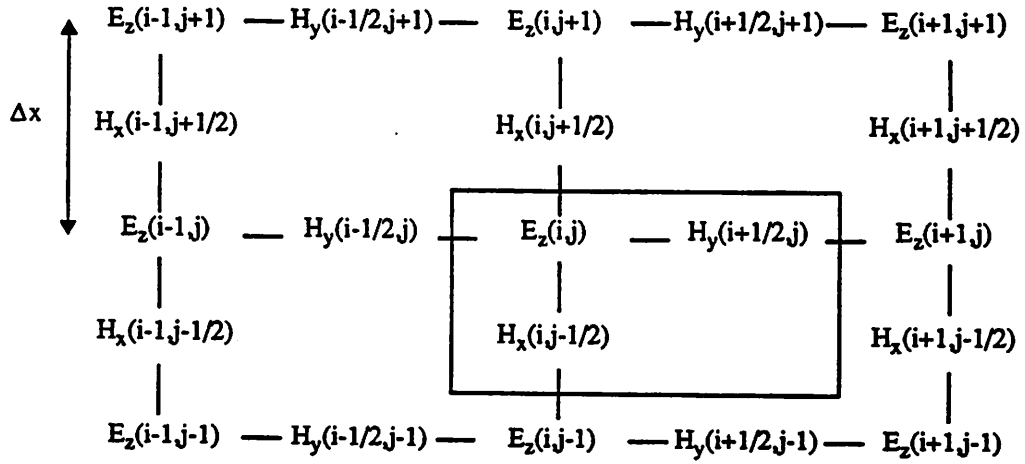


Figure 2.2 Discretization of the simulation domain for the TE polarization. Three field components inside the box collectively constitute one simulation node.

The TE polarization is defined such that the electric field is parallel to all surfaces of the simulation domain.

The resulting discretization scheme of the two dimensional simulation domain is shown in Figure 2.2 where the three field components inside the box (E_z , H_x and H_y) constitute one simulation node. Each simulation node contains three field components: the electric field in the z-direction (E_z), and the magnetic field in the x- and y-directions (H_x and H_y). The time-domain finite-difference solution to such a problem had been presented by Gamelin et al.⁸ and is repeated here:

$$E_z^{n+1}(i, j) = \frac{1}{\frac{\sigma \Delta x}{2} + \frac{\epsilon \Delta x}{\Delta t}} \left(H_x^{n+\frac{1}{2}}(i, j - \frac{1}{2}) - H_x^{n+\frac{1}{2}}(i, j + \frac{1}{2}) + H_y^{n+\frac{1}{2}}(i + \frac{1}{2}, j) - H_y^{n+\frac{1}{2}}(i - \frac{1}{2}, j) \right) - \frac{\frac{\sigma \Delta x}{2} - \frac{\epsilon \Delta x}{\Delta t}}{\frac{\sigma \Delta x}{2} + \frac{\epsilon \Delta x}{\Delta t}} E_z^n(i, j) \quad (2.6)$$

$$H_y^{n+\frac{1}{2}}(i + \frac{1}{2}, j) = H_y^{n-\frac{1}{2}}(i + \frac{1}{2}, j) + \frac{\Delta t}{\mu \Delta x} [E_z^n(i + 1, j) - E_z^n(i, j)] \quad (2.7)$$

$$H_x^{n+\frac{1}{2}}(i, j - \frac{1}{2}) = H_x^{n-\frac{1}{2}}(i, j - \frac{1}{2}) + \frac{\Delta t}{\mu \Delta x} [E_z^n(i, j - 1) - E_z^n(i, j)] \quad (2.8)$$

A second order absorbing boundary condition at the top boundary is⁹:

$$\begin{aligned} E_z^{n+1}(i, Y) = & E_z^n(i, Y - 1) - \left(\frac{c\Delta t - n\Delta x}{c\Delta t + n\Delta x} \right) E_z^n(i, Y) + \frac{\mu c^2 \Delta t}{2n(c\Delta t + n\Delta x)} \times \\ & \left(H_y^{n+\frac{1}{2}}(i + \frac{1}{2}, Y - 1) - H_y^{n+\frac{1}{2}}(i - \frac{1}{2}, Y - 1) + H_y^{n+\frac{1}{2}}(i + \frac{1}{2}, Y) - H_y^{n+\frac{1}{2}}(i - \frac{1}{2}, Y) \right) + \\ & \left(\frac{c\Delta t - n\Delta x}{c\Delta t + n\Delta x} \right) E_z^{n+1}(i, Y - 1) \end{aligned} \quad (2.9)$$

where the superscripts of the field variables stand for the time step and the subscripts represent the direction of the field, i and j are respectively the x - and y -coordinate of an arbitrary node and Y is the y -coordinate at the top boundary, Δx and Δt are the spatial and temporal discretization units, ϵ , μ , σ , and n are the (constant) permittivity, permeability, conductivity and refractive index of the material, respectively. Equation (2.9) can be generalized to other boundaries of the simulation domain with suitable coordinate transformations.

2.3 Extension to the TM Polarization

In the TM polarization, the magnetic field is parallel to all surfaces of the two-dimensional simulation domain. Therefore, the magnetic field has only one component in the z -direction (H_z), and the electric field has two components in the x - and y -directions (E_x and E_y). This is symmetric to the TE polarization with the substitution of the electric field by the magnetic field and vice versa. The only asymmetry between the two polarizations is the lack of magnetic conductivity. Hence, the discretized equations for the TM polarization cannot be obtained directly from those of the TE polarization (equations (2.6), (2.7), (2.8), and (2.9)) by the substitutions $E \rightarrow H$, $H \rightarrow E$, $\epsilon \rightarrow -\mu$, and $\mu \rightarrow -\epsilon$. Instead, the discretized equations for the TM polarization must be derived from the Maxwell's equations (equations (2.1) and (2.2)). The resulting equations are

$$H_z^{n+1}(i, j) = -\frac{\Delta t}{\mu \Delta x} \left(E_x^{n+\frac{1}{2}}(i, j - \frac{1}{2}) - E_x^{n+\frac{1}{2}}(i, j + \frac{1}{2}) + E_y^{n+\frac{1}{2}}(i + \frac{1}{2}, j) - E_y^{n+\frac{1}{2}}(i - \frac{1}{2}, j) \right) + H_z^n(i, j) \quad (2.10)$$

$$E_y^{n+\frac{1}{2}}(i + \frac{1}{2}, j) = -\frac{\frac{\sigma \Delta x}{2} - \frac{\epsilon \Delta x}{\Delta t}}{\frac{\sigma \Delta x}{2} + \frac{\epsilon \Delta x}{\Delta t}} E_y^{n-\frac{1}{2}}(i + \frac{1}{2}, j) - \frac{1}{\frac{\sigma \Delta x}{2} + \frac{\epsilon \Delta x}{\Delta t}} [H_z^n(i + 1, j) - H_z^n(i, j)] \quad (2.11)$$

$$E_x^{n+\frac{1}{2}}(i, j - \frac{1}{2}) = -\frac{\frac{\sigma \Delta x}{2} - \frac{\epsilon \Delta x}{\Delta t}}{\frac{\sigma \Delta x}{2} + \frac{\epsilon \Delta x}{\Delta t}} E_x^{n-\frac{1}{2}}(i, j - \frac{1}{2}) - \frac{1}{\frac{\sigma \Delta x}{2} + \frac{\epsilon \Delta x}{\Delta t}} [H_z^n(i, j - 1) - H_z^n(i, j)] \quad (2.12)$$

and a second order boundary condition at the top boundary is⁹

$$H_z^{n+1}(i, Y) = H_z^n(i, Y - 1) - \left(\frac{c\Delta t - n\Delta x}{c\Delta t + n\Delta x} \right) H_z^n(i, Y) - \frac{(\epsilon + \sigma\Delta t)c^2\Delta t}{2n(c\Delta t + n\Delta x)} \times \left(E_y^{n+\frac{1}{2}}(i + \frac{1}{2}, Y - 1) - E_y^{n+\frac{1}{2}}(i - \frac{1}{2}, Y - 1) + E_y^{n+\frac{1}{2}}(i + \frac{1}{2}, Y) - E_y^{n+\frac{1}{2}}(i - \frac{1}{2}, Y) \right) + \left(\frac{c\Delta t - n\Delta x}{c\Delta t + n\Delta x} \right) H_z^{n+1}(i, Y - 1) \quad (2.13)$$

2.4 Implementation

Despite the asymmetries between the TE and the TM polarizations, the forms of the equations for the TM and TE polarizations are identical. Therefore, one iteration routine is adequate for both polarizations. During the n^{th} time step, the field value of any node can be expressed as a sum of its neighboring values and its value at the $(n-1/2)^{\text{th}}$ and $(n-1)^{\text{th}}$ time steps, i.e.,

$$V^n(i, j) = \sum_{l=-1/2, 0, 1/2; m=-1/2, 0, 1/2; k=1/2, 1} a_{lmk} V^{n-k}(i + l, j + m) \quad (2.14)$$

where $V^n(i, j)$ is any field variable value at the n^{th} time step at the two-dimensional grid location (i, j) , and a_{lmk} is the multiplicative coefficient which depends on the polarization. For example, the equations (2.7) and (2.11) can be written in the form

$$F_y^{n+\frac{1}{2}}(i + \frac{1}{2}, j) = a F_y^{n-\frac{1}{2}}(i + \frac{1}{2}, j) + b [F_z^n(i + 1, j) - F_z^n(i, j)] \quad (2.15)$$

where F_y and F_z represent the electric field in the y-direction and the magnetic field in the z-direction for the TM polarization, and vice versa for the TE polarization. The coefficients a and b are given by

$$a = -\frac{\frac{\sigma\Delta x}{2} - \frac{\epsilon\Delta x}{\Delta t}}{\frac{\sigma\Delta x}{2} + \frac{\epsilon\Delta x}{\Delta t}} \text{ and } b = -\frac{1}{\frac{\sigma\Delta x}{2} + \frac{\epsilon\Delta x}{\Delta t}} \text{ for the TM polarization, and} \quad (2.16)$$

$$a = 1 \text{ and } b = \frac{\Delta t}{\mu\Delta x} \text{ for the TE polarization.} \quad (2.17)$$

Therefore, the iteration routine contains updating equations of the form similar to equation (2.15), with values of the multiplicative coefficients depending on the polarization. Thus, the computer time required per iteration is the same for both polarizations, although the total simulation time (a quantity which is proportional to the number of wave cycles for convergence) may differ depending on the structures being simulated.

Chapter 3

Oblique Incidence

3.1 Introduction

Although TEMPEST simulation and experimental comparisons have shown that many optical scattering and imaging issues can be modeled reasonably well with normally incident illumination, the effects of oblique incidence must be understood in order to study rigorously phenomena such as partial coherence. Not only do the boundary conditions become more complex, simulation of off-axis effects with a time-domain, finite-difference approach is complicated by the existence of a phase difference across the top boundary of the simulation domain. Nevertheless, the use of a periodic structure such that there is a $m2\pi$ phase difference between the east and west boundaries greatly simplifies the problem. Another complication of oblique incidence analysis is the need to synchronize the analytically calculated sinusoidal excitation function with the numerically propagated field. Modification of the dispersion relation as well as proper excitation of the simulation domain are necessary for synchronization.

3.2 Left-right Periodic Boundary Condition

In general, the field components at the left and right boundaries differ in both amplitude and phase. If the simulated structure is assumed to be periodic, however, the amplitudes of the field components are equal at the east and west boundaries. Nevertheless, this assumption alone does not simplify the algorithm because phase difference may still exist between the left and right boundaries. With the additional assumption that the phase difference is zero (modulo 2π) between the two side boundaries, no modification for the field equations is necessary for oblique incidence. The assumption of zero (modulo 2π) phase difference means that depending on the horizontal dimension of the simulation domain and the illumination wavelength, only discrete values of the illumination angle are allowed. If the horizontal period of a periodic structure is d and the illumination wavelength is λ as shown in Figure 3.1, then

the phase difference between the left and right boundaries of the simulation domain is zero (modulo 2π) for illumination angles given by

$$m\lambda = d \sin \theta \quad (3.1)$$

where m is any integer. From equation (3.1), it can be seen that the allowed illumination directions are the directions of the diffraction harmonics. Although only discrete values of incident angles are allowed in this simplification, TEMPEST is still useful for off-axis incidence simulations because for most applications in photolithography, it has the computational power to make the period of the simulation domain several times larger than the lateral dimension of the structure under study. Thus, the diffraction harmonics can be sampled at angular intervals small compared to the angular dependence associated with the topography itself. This is true for both isolated and periodic structures. For an isolated structure, there is no theoretical limit to the horizontal dimension of the simulation domain so that the desired fineness of the angular dependence can be obtained. For a periodic structure, the same fineness can be obtained by including several periods of the structure inside the simulation domain.

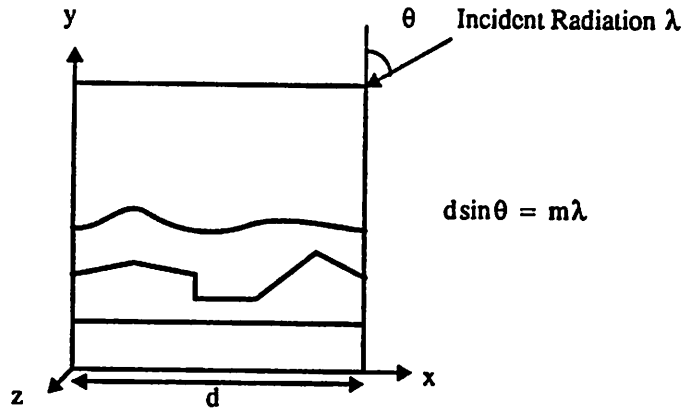


Figure 3.1 Left-right periodic boundary condition for oblique incidence. Only discrete angles of illumination which satisfy the relation in equation (3.1) are allowed.

3.3 Domain Excitation

Although no modification is necessary for the field equations, care must be exercised when applying the sinusoidal excitation function to the simulation domain. This is because any initial synchronization error existing at the boundary nodes between the analytically calculated sinusoidal excitation function and the numerically propagated wave will be magnified as simulation proceeds and will lead to numerical instability. There are two types of synchronization errors: field value mismatch and dispersion relation error. Field value mismatch is discussed in this section and dispersion relation error will be discussed in Section 3.4.

For oblique incidence, the existence of a phase difference between successive simulation nodes creates difficulty for the numerical boundary condition at the top of the simulation domain. Since the incident field values vary between successive simulation nodes on the top row, synchronization error results if the field variables of all simulation nodes are initialized to zero. This is because any non-uniformity of difference between the incident field and the initial field values across the top boundary of the simulation domain is coupled into the absorbing boundary condition. This non-uniformity is magnified as simulation proceeds, and will eventually lead to numerical instability. To achieve synchronization, the difference in values between the incident field variables and the field variables must be constant across the top boundary at $t=0$. A simple way to achieve this is to initialize the field variables several rows lower into the simulation domain with the incident field values (both the electric and the magnetic fields). In this way, the difference in values between the analytical excitation function and the numerical field variables is uniformly zero across the top of the simulation domain. There is no synchronization error at the boundary nodes and therefore no numerical instability. Although synchronization error exists at the row of simulation nodes where the values of the field variables drop abruptly from the incident field values to zero, this error will decay instead of grow because it is

not coupled to the boundary nodes (and hence the boundary conditions). Eventually, this synchronization error existing initially in the bulk of the simulation domain will be absorbed by the absorbing boundary conditions.

3.4 Dispersion Relation

The other source for synchronization error is the difference in dispersion relation between a wave propagating in continuous time and space and one propagating in discrete time and space. For a wave propagating in continuous time and space, the dispersion relation is given by

$$k = \frac{\omega}{c} = \frac{2\pi}{\lambda} \quad (3.2)$$

However, the dispersion relation for a wave propagating in discrete time and space with wavelength λ is¹⁰

$$\frac{1}{c\Delta t} \sin\left(\frac{1}{2}\omega\Delta t\right) - \left(\frac{1}{\Delta y^2} \sin^2\left(\frac{1}{2}k_y\Delta y\right) - \frac{1}{\Delta x^2} \sin^2\left(\frac{1}{2}k_x\Delta x\right) \right)^{1/2} = 0 \quad (3.3)$$

where the relation between λ and ω is still given by equation (3.2). Although the difference between equations (3.2) and (3.3) is slight, it is important that equation (3.3) is used to determine the wave numbers for the analytically calculated sinusoidal excitation. From experience, if equation (3.2) is used instead, the excitation function and the numerical wave will eventually go out of sync, and the diffraction efficiencies calculated may be inaccurate.

For implementation in TEMPEST, the wave number in the x-direction is calculated first according to

$$k_x = k_0 \sin\theta \quad (3.4)$$

where k_0 is the continuous time wave number given by equation (3.2) and θ is the incident angle. With the value of k_x calculated from equation (3.4), the value of k_y can then be determined from equation (3.3).

Chapter 4

Image Synthesis

4.1 Motivation

The assumption of coherent illumination in TEMPEST is not realistic. Optical image profiles for a coherent system often show large ringing amplitudes which are either smaller or not present at all in incoherent and partial coherent systems. Partial coherent imaging can be modeled in TEMPEST with oblique incidence by superposing simulation results for different angles of illumination. This approach, although accurate and feasible, generally requires a lot of simulation runs and is inefficient. Therefore, given the characteristics of an optical system, it is desirable if partial coherent effects can be approximated using TEMPEST simulation results for normal (or at most a few angles of) incidence.

4.2 Formulation

If the magnitude of the diffraction efficiencies is independent of the incident angle, and if the illumination energy is uniformly distributed over the illumination cone of an optical system, then the optical image profile of a structure can be calculated by weighing each pair of diffraction harmonics by their overlapping area with the collection cone as shown in Figure 4.1. This method is similar to Hopkins' approach¹¹ and can be used to model bright-field or dark-field optical systems as well as defocus effects. Extensions to non-uniform illumination systems as well as slowly varying diffraction efficiencies (with angle of incidence) are easily generalized.

With the two assumptions stated above, the intensity at any point (x,y) in the two-dimensional space can be calculated by the integral

$$I(x, y) = \frac{1}{C} \int_{\Omega} \frac{1}{2\rho} \sum_{i,n} \cos \theta_n [(\hat{A}_i \hat{A}_n + \hat{B}_i \hat{B}_n) \cos [(\hat{k}_n - \hat{k}_i) \cdot \hat{r}]] d\Omega + \frac{1}{C} \int_{\Omega} \frac{1}{2\rho} \sum_{i,n} \cos \theta_n [(\hat{B}_i \hat{A}_n - \hat{A}_i \hat{B}_n) \sin [(\hat{k}_n - \hat{k}_i) \cdot \hat{r}]] d\Omega \quad (4.1)$$

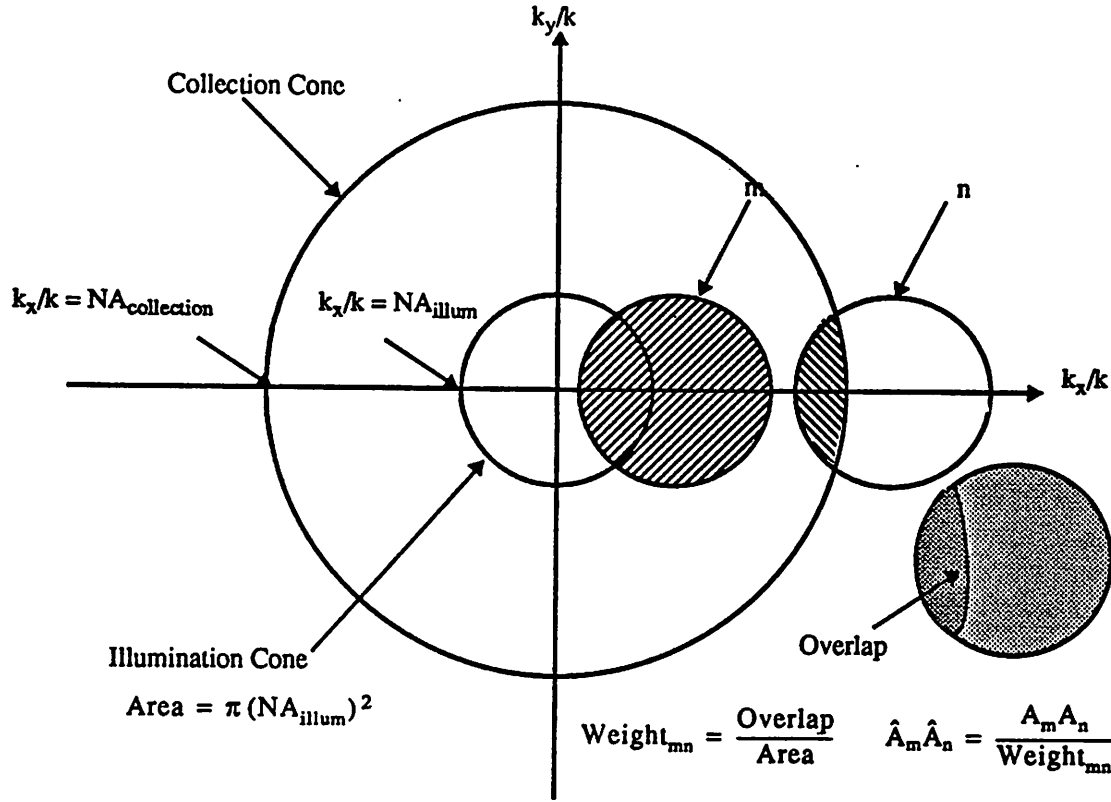


Figure 4.1 Image synthesis based on Hopkins' approach. To each diffraction harmonic corresponds a circle in the normalized k -space with its area the same as that of the illumination cone. The center for each circle is located at $k_x/k = n(\lambda/p)$ and $k_y/k = 0$, where n is the order of the diffraction harmonic, λ is the wavelength, and p is the period of the simulation domain. The weighing coefficient of each pair of diffraction harmonics is proportional to the overlapping area of their corresponding circles with the collection cone in normalized k -space.

where $\vec{r} = (x_i, y_j)$ and the summation is over all diffraction harmonics. The diffraction harmonics are actually a finite Fourier series (only the propagating modes are included in the expansion) of the electric field. The \hat{A}_i 's and \hat{B}_i 's are the weighed Fourier coefficients of the sine and cosine terms respectively. The variable p is equal to the intrinsic impedance η for the TE polarization, and is equal to the inverse of the intrinsic impedance $1/\eta$ for the TM polarization. C is the area of the illumination circle of the optical system in normalized k -space.

4.3 Validity of the Assumptions

The assumption of uniformly distributed energy over the illumination cone is reasonable for optical light sources. For some laser sources, however, this assumption may not be valid due to the presence of speckle. Nevertheless, when such sources are used for exposure, the same area of the photoresist is usually exposed several times to reduce the speckle effects. Therefore, it is still reasonable in most applications to assume that the average of the exposures has a uniform energy distribution.

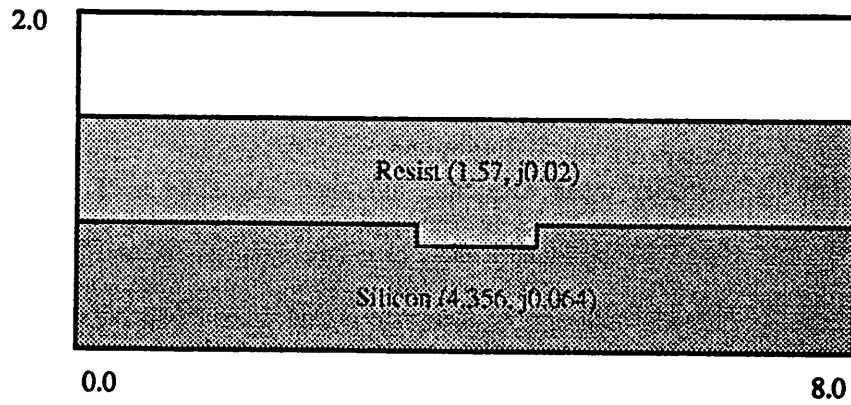


Figure 4.2 Alignment mark structure used in the study of oblique incidence. The mark is 600 nm wide and 150 nm deep. The period of the simulation domain is 8.0 μm .

Intuitively, the assumption of constant diffraction efficiencies with respect to illumination angle should be valid for small angles. However, the smallness of the incident angle requires quantification. First consider the alignment mark structure shown in Figure 4.2. The mark is 600 nm wide (1.2λ) and 150 nm deep (0.3λ) and is illuminated with monochromatic radiation of freespace wavelength at 0.488 μm . From equation (3.1), for $m2\pi$ phase difference between the left and right boundaries, angular steps of about 3.5° can be used. The results of simulations done with this alignment mark in Figure 4.3 show that the magnitude of the diffraction efficiencies are more or less constant for illumination angles less than 40° . This correspond to an NA of about 0.65, larger than the numerical

aperture used in the alignment collection optics for this application. Thus for this application, only the diffraction efficiencies calculated for normal incidence are necessary.

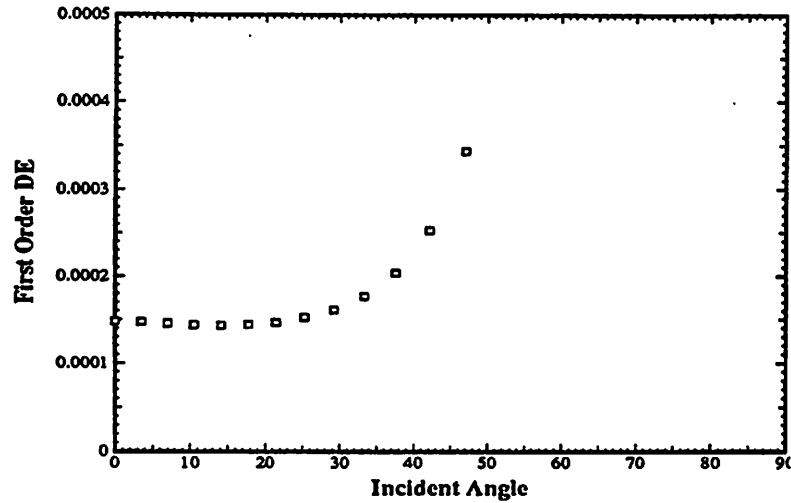


Figure 4.3 First order diffraction efficiency magnitude as a function of the incident angle for an alignment mark. The magnitude is more or less constant for incident angles less than about 40°. The increasing trend at higher angles of incidence is due probably to the imperfectness of the boundary conditions.

In other applications, diffraction calculations at several oblique angles may be necessary. A measure of a reasonable step size can be determined by drawing the parallelism between electromagnetic scattering of silicon wafer structures and antenna theory. For a rectangular aperture with uniform aperture distribution of length a , the half-power width in degrees is¹²

$$\Delta\theta = 51^\circ (\lambda/a) \quad (4.2)$$

Angular steps three or four times smaller than $\Delta\theta$ would likely be adequate. The angles allowed in TEMPEST simulations are given by $m\lambda = d \sin \theta$ (equation (3.1)). Using the small angle approximation and converting radians to degrees gives

$$\Delta\theta_{\text{TEMPEST}} = 57^\circ (\lambda/d) \quad (4.3)$$

Thus, choosing the period four times the structure size ($d \geq 4a$) gives angular steps about four times smaller than the full width half maximum bandwidth as desired. Since in most applications the period d is a parameter which can be freely chosen for simulation purposes, increased angular accuracy can be obtained.

Chapter 5

Current Status of TEMPEST

TEMPEST version 2.0 described in this thesis has several key extensions from the previous version (version 1.0). The changes range from electromagnetic aspects to user interface and auxiliary supporting tools. The electromagnetic aspects of the extended program are discussed in the previous chapters. In this chapter, these added capabilities are summarized and the improved user interface and auxiliary supporting tools are described.

In TEMPEST version 2.0, transverse magnetic (TM) problems can be analyzed in addition to transverse electric (TE) problems. Oblique incidence at discrete angles is also an additional feature in version 2.0. Further, TEMPEST version 2.0 has been extended to allow for arbitrary material as the top layer of the simulation domain. Previously, only vacuum was allowed as the first layer of the simulation domain.

In version 1.0, only output data of the diffraction harmonics, the electric field values and the absorbed energy in the photoresist are available. Version 2.0 can provide data on the magnetic field as well as the electric field, non-steady-state fields and steady-state fields, transient fields, field amplitudes and instantaneous field values, absorbed energy in the photoresist, and the diffraction harmonics.

Besides the enhanced computing capabilities, TEMPEST version 2.0 is easier to use than the previous version. It can be executed just as an ordinary program. In TEMPEST version 1.0, prior to running the program each time, the user must load the object code and compile the program, a process which is both tedious and time-consuming. With the current version 2.0, the executable binary code of TEMPEST can be placed in any directory and can be accessed from anywhere in the system by just setting the PATH variable. The process of running TEMPEST version 2.0 thus becomes simpler and more convenient. The user can telnet or remote login to a front-end machine of a CM to run TEMPEST from any workstation or even a personal computer with network access. Further, simulations

with TEMPEST version 2.0 can be submitted as batch jobs. Thus, the user can utilize the unix command `at` to send the simulation runs to a queue of the CM, thereby removing the necessity to sit in front of a terminal and wait for a free sequencer.

In addition, as TEMPEST version 2.0 is written in C* instead of *lisp in version 1.0, file manipulation is easier in the current version. Comments are allowed in the input file, and the format is more flexible because the entries of the input file can occur in random order. In version 1.0, the input file to TEMPEST must be given the name "topog.d" and the output files are named "de.o," "e-val.o," and "m-val.o." This rigid naming convention has changed in version 2.0. The input files read by TEMPEST and output files produced by TEMPEST can be given any user specified name.

Besides the main electromagnetic fields solver program, TEMPEST version 2.0 includes several auxiliary programs. The geometry previewing program SHAPE allows the user to preview the topography and check for possible errors in the input file. The image synthesis program IMAGE has been refined. It models partial coherent effects of the optical system based on Hopkins' approach. Other routines such as CONVERT and FACTOR are used for output data processing. These routines are explained in detail in the users' guide of TEMPEST version 2.0.

Chapter 6

Applications to Mask Transmission*

6.1 Abstract

Polarization and interface reflection effects are examined for four mask making technology issues: chrome edge shape, overcoating, double phase-shifting removal of defects, and reflective masks. This study is based on the massively parallel rigorous electromagnetic simulator TEMPEST, with extensions to include the TM polarization and boundary conditions for outgoing waves in optical materials. The analysis was carried out on a CM-2 connection machine with remote electronic access. A local workstation was used to write and preview the geometry as well as process images from files of diffraction efficiencies downloaded to the workstation from the network. Through this remote analysis procedure, the four proto-typical mask case studies described by Doi et al.⁶ were examined for polarization and boundary condition effects.

For chrome masks of one wavelength wide opening in a 1X system at 0.248 μm , moderate differences between the TE and the TM polarizations were observed in the peak intensities (10%). The TM polarization in general showed higher transmission and lower sidelobes. The two polarizations showed a similar increase in linewidth and peak intensity with decreasing chrome edge slope. The difference was not as pronounced for a 5X system at 0.365 μm . Overcoating chrome masks with anti-reflection layers improved resolution for both polarizations. For 5X chromeless phase-shifting masks at 0.365 μm , neither polarization effect nor phase-shifter edge slope was important. The peak intensity at the phase-shifting section changed by only 1% and the linewidth varied by less than 2% when the phase-shifter edge slope changed from 90° to 45°, keeping the mid-points of the phase-shifter edge fixed. To remove defects on such masks by double phase-shifting may drop the intensity level to 70% of the clear field value for

* This chapter is extracted from the author's published paper "Polarization Effects in Mask Transmission," *Proc. SPIE, Optical/Laser Microlithography*, vol. 1674, pp. 193-200, Mar., 1992.

a $0.1 \lambda/NA$ sized defect. For 1X reflective masks at one wavelength, both polarizations displayed similar behaviors. These reflective masks with built-in material-based phase-shifting improved the image slope, and the TM polarization was found to have slightly less ringing than the TE polarization.

6.2 Introduction

With the introduction of new technologies and with the scaling of optical lithography, the printability of small features on masks has become more important. In 1X optical systems, not only is transmission through a wavelength-sized aperture a concern, differences in optical image quality between the transverse electric (TE) and the transverse magnetic (TM) polarizations are important. In reduction systems, polarization effects due to diffraction from masks may not be as significant as in 1X systems. For reduction systems, material effects such as overcoating may affect image quality significantly. There is also evidence that improvement in resolution can be obtained by overcoating chrome masks with a transparent layer¹³. In addition to the conventional chrome masks, chromeless phase-shifting masks have attracted increasing attention in recent years. Besides the effects of phase-shifting mask edges on optical image quality, the feasibility of defect removal of such masks by double phase-shifting, i.e., to have 0° - 360° transitions which do not significantly affect the intensity level, is another concern¹⁴. The possibility of built-in material-based phase-shifting in reflective masks¹⁵ also deserves attention.

This paper examines polarization effects in four technology issues in scaling optical projection printing to smaller feature sizes. The following technology issues are assessed: chrome edge shape effects, mask overcoating effects, phase-shifting material edge effects, and reflective masks.

6.3 Simulation Techniques

A typical simulation domain for a chrome mask is shown in Figure 6.1 with a chrome ($n=[4.02,2.11]$) thickness of 80 nm. The domain is $2 \mu\text{m}$ by $2 \mu\text{m}$ using 512 simulation nodes on each side. This results in a grid of

3.9 nm between nodes. For an illumination wavelength of $0.248\ \mu\text{m}$, this translates to almost 16 simulation nodes per wavelength in the optically densest material of the structure (chrome), more than the nominal 10 nodes per wavelength rule of thumb⁸ for accuracy. With the extension to allow for arbitrary dielectric material at the top, the domain is excited in the glass instead of in air as was done previously. The electric field generally reaches steady-state 30 wave cycles after the initial excitation. This requires about five minutes on an 8k CM-2 machine.

6.4 Chrome Edge Effects

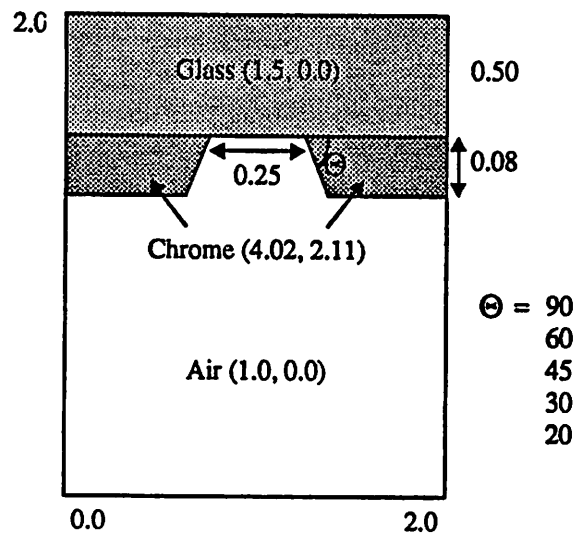


Figure 6.1 A typical simulation domain for a chrome mask. The normally incident plane wave interacts with the mask and produces a transmitted field at the bottom.

To study polarization differences in the effects of chrome edge shapes, five masks similar to those considered by Doi et al.⁶ were simulated. The basic structures of the chrome masks are shown in Figure 6.1 with chrome edge slopes of 90° , 60° , 45° , 30° and 20° , and the chrome opening width next to the glass fixed. For a 1X mask in deep-UV ($\lambda = 0.248\ \mu\text{m}$, $\text{NA}=0.7$, $\sigma = 0.5$), the opening width was $0.25\ \mu\text{m}$, about one wavelength wide. The peak intensities and linewidths of both polarizations increased as the edge slope was decreased. This increase may be attributed to the penetration of fields into the thinner portion of the chrome. The sensitivity of peak intensity to edge

slope is about the same for both polarizations. Plotting the square root of the intensity in Figure 6.2 shows the sidelobe behavior in detail. The TE polarization has the highest sidelobes which might be expected from concentration of currents on the chrome edges. The taper helps to reduce these sidelobe effects.

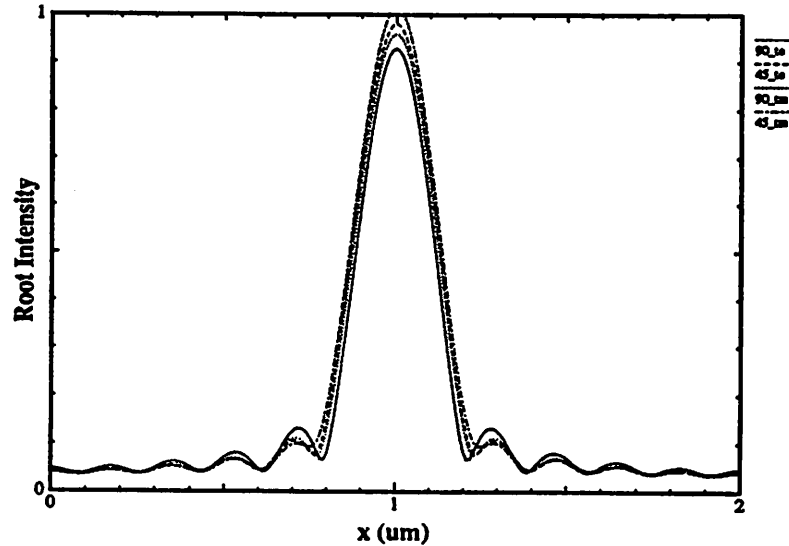


Figure 6.2 Square root of the intensities of chrome masks with edge slopes of 90° and 45° for the TE and TM polarizations. The TE polarization shows higher sidelobes and lower peak intensities.

The behavior in Figure 6.2 shows that for narrow slits with the same chrome edge slope, the peak intensity of the TM polarization was higher than that of the TE polarization. In order to further investigate the differences between the two polarizations for narrow slit diffraction, chrome masks with vertical edges of different space widths were simulated and compared with the scalar diffraction approach of SPLAT¹⁶. Figure 6.3 shows optical image profiles from different approaches for a particular chrome opening width of 0.20 μm . The curve labeled SPLAT shows simulation results from the scalar diffraction theory. VP_C_TE and VP_C_TM are respectively peak intensities from TEMPEST simulations of scattering through a 0.20 μm opening in chrome for the TE and TM polarizations. Also shown in the figure are the VP_A_TE and VP_A_TM curves which are for vector propagation across the domain of an assumed square wave aperture illumination. The images were synthesized from TEMPEST simulation results for

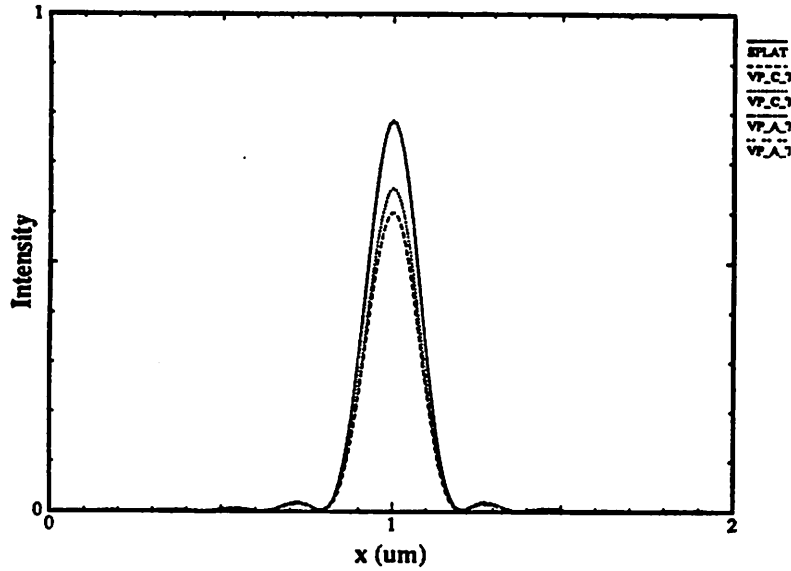


Figure 6.3 Simulated Images from SPLAT and TEMPEST for a chrome mask of space width $0.20\ \mu\text{m}$. The scalar approach of SPLAT shows a higher peak intensity.

an empty domain excited by a $0.20\ \mu\text{m}$ wide coherent source. The optical image profile from SPLAT and both the VP_A curves are calibrated by multiplying their intensities by the glass to air transmission factor of 0.96. These three profiles almost coincide. This is expected because in the limit of a perfect mask, there should be no difference between SPLAT and TEMPEST. For scattering through a chrome mask, however, the VP_C_TE and VP_C_TM curves show lower peak intensities than the SPLAT image. This loss in peak intensity is apparently due to a combination of propagation through small apertures and energy dissipated in the chrome.

To investigate transmission effects as a function of polarization, the partial coherence effects in imaging must be separated from the aperture resonance effects. To remove the former effect, we consider in Figure 6.4 the total energy transmitted normalized to the opening width and the energy which would be transmitted in a large clear field. The TM polarization shows that more energy is transmitted for all sizes and is significantly larger in the small opening region. The higher peak intensity for the TM polarization may be traced to the boundary conditions at the air-chrome interface¹⁷. Assuming that chrome is a perfect conductor, electric field parallel to and magnetic field perpendicular to

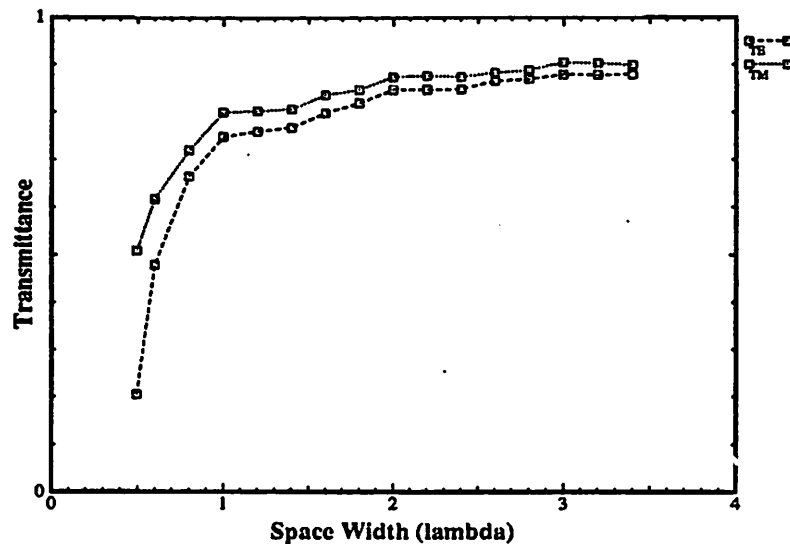


Figure 6.4 Transmission of a narrow opening normalized to the opening width and the energy which would be transmitted in a large clear field. The TM mode always shows higher transmission than the TE mode for chrome masks. Resonances occur at opening widths equal to integral multiples of free space wavelength. The low transmission for small opening widths indicates that scattering from the glass edges are important in reducing transmission for small apertures.

the chrome edges are zero. In the TE polarization (electric field parallel to the chrome edge), these boundary conditions require that both E_z and H_x vanish at the chrome edges. In the TM polarization, however, H_z and E_x can be non-zero at the chrome edges. Consequently, more energy can pass through in the TM mode since the field amplitude is larger. Energy consideration in the “waveguide” between the chrome edges leads to the same conclusion.

Notice also in Figure 6.4 that for both polarizations, the energy transmitted shows a periodic variation of about 6%. The peaks occur at chrome opening widths of approximately $0.25 \mu\text{m}$, $0.5 \mu\text{m}$, and $0.75 \mu\text{m}$, with minima at $0.35 \mu\text{m}$ and $0.6 \mu\text{m}$. These are almost exact periodic distances and correspond to full and half wave distances between the two edges as viewed in air. This resonance phenomenon appears to arise from constructive and destructive interference of re-radiation of resonant currents on the two chrome edges.

For a 5X system ($\lambda = 0.365\mu\text{m}$, $\text{NA}=0.42$, $\sigma = 0.5$), peak intensity variations as well as polarization effects were less pronounced. The optical parameters at $0.248\mu\text{m}$ were used in the simulations for comparison purposes. The width of the chrome opening in these 5X masks is $2.5\mu\text{m}$ at the small opening next to the glass. For slopes as low as 45 degrees, the maximum increase in peak intensity is 4.6% for the TE polarization and is 2.3% for the TM polarization. The difference between the two polarizations is 2.8%. For reduction systems, polarization and chrome edge effects are not likely to be significant especially if as is often done, a single experimentally determined print bias factor per edge is added in layout or mask design.

6.5 Mask Overcoating Effects

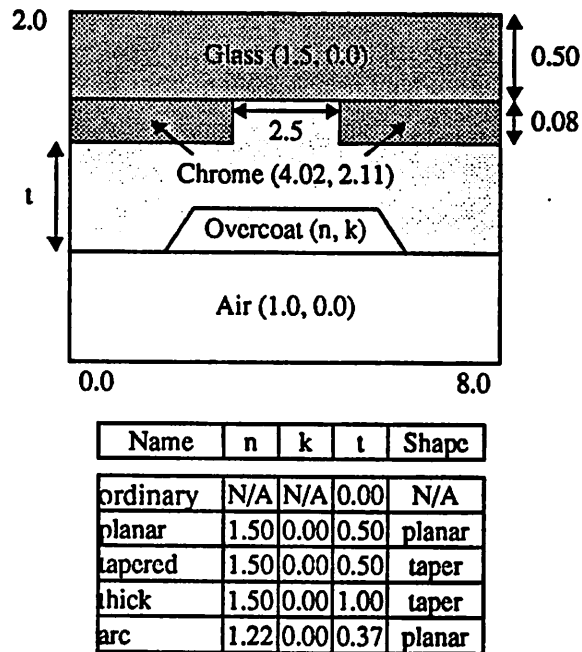


Figure 6.5 Several geometries representing possible overcoating topographies used in TEMPEST simulation.

Doi et al.⁶ considered several mask overcoating geometries and materials, and found effects of about 10% in the peak values of the image intensity. Since intensity variations of this level may be confounded by effects of artificial reflections with the glass mask layer simulated, a further investigation was required. To eliminate inter-layer

reflections, new boundary conditions were developed such that waves could exit from the glass layer at the top. Five masks were then studied, consisting of: (a) no overcoating, (b) planar coating of oxide ($n=[1.5, 0.0]$) of $0.5 \mu\text{m}$ thick, (c) oxide coating with a tapered edge at the chrome opening, (d) a thick oxide coating of $1.0 \mu\text{m}$ thick with a tapered edge, and (e) a planar anti-reflection coating ($n=[1.22, 0.0]$) of thickness equal to five quarters of the wavelength. These five cases are shown in Figure 6.5.

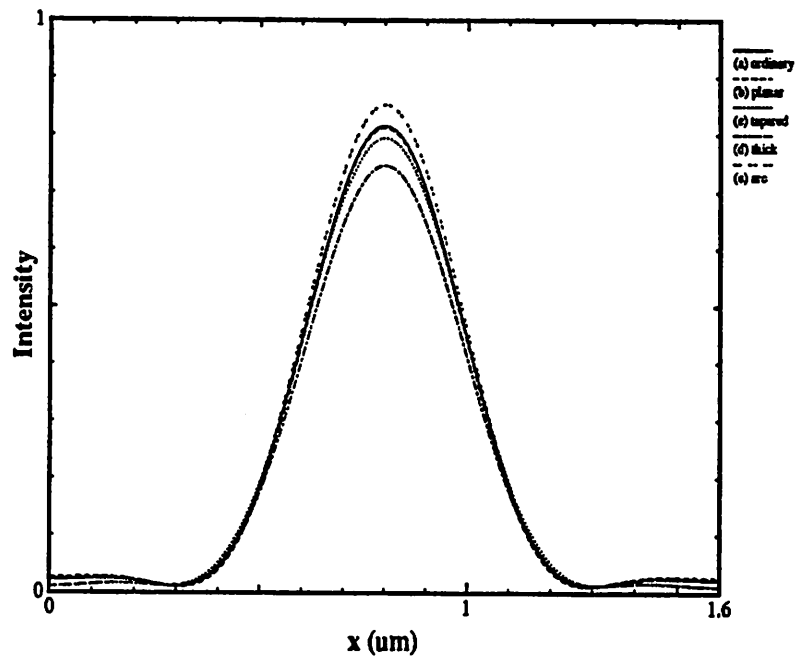


Figure 6.6 Images of the five overcoating geometries for the TE polarization. Only the anti-reflection overcoating (arc) increases the peak intensity.

Images corresponding to these overcoating geometries are shown for the TE and TM polarizations in Figure 6.6 and Figure 6.7 respectively. Simulations were conducted for a 5X stepper at i-line ($\lambda = 0.365 \mu\text{m}$, $\text{NA}=0.42$, $\sigma = 0.5$). For both polarizations, the peak intensities were the highest for anti-reflection overcoating. However, all the peak intensities of masks with oxide overcoating were less than that of no overcoating. Thick oxide overcoating layers produced the most reduction in intensity, whereas planar overcoating produced the least change in intensity. Tapered overcoating reduced the peak intensity more than planar overcoating did. This suggests that the tapered edge

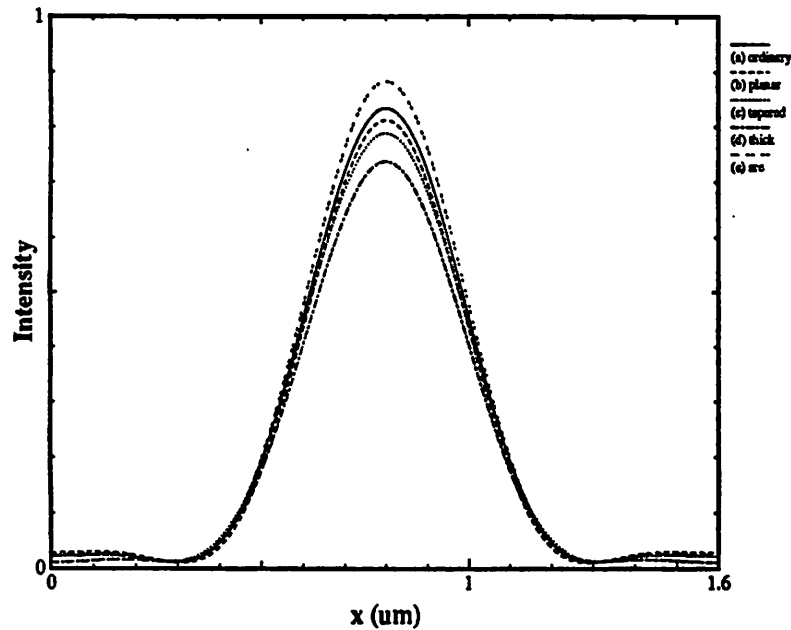


Figure 6.7 Images of the same overcoating geometries as Figure 6.6 for the TM polarization. Both polarizations display similar behaviors.

of the overcoating layer creates a diverging lens-like effect or additional scatterers and hence reduces the peak intensity. Another contribution to the reduction of peak intensity of oxide overcoated masks may be reflection loss between the oxide-air interface and the oxide-chrome interface after light is diffracted through the aperture. It appears that transmission can be enhanced primarily by reducing reflection. Thus, an anti-reflection overcoat results in the highest peak intensity by eliminating the undesired reflection and increases the peak intensity.

The optical image profiles were almost the same for both polarizations in the cases where the overcoating layer caused a reduction in intensity. However, for the non-overcoated and for the anti-reflection overcoated structures, the TM polarization showed higher peak intensities than the TE polarization. In fact, the relative transmission of the TM polarization is increased much more than that of the TE polarization. This may be explained by postulating that the diffracted waves in the TM polarization, traveling at a non-zero angle with respect to the dielectric interface, have a smaller reflection coefficient than the TE polarization.

6.6 Phase-shifting Material Edge Effects

In chromeless phase-shifting masks, abrupt changes in phase-shifter thickness in the neighboring region between the phase-shifting and the non-phase-shifting sections may give rise to a host of problems. To produce a 180° phase shift, a change in thickness of $(\lambda/(2(n-1)))$ is required. A typical phase-shifting material is glass of refractive index 1.5. This translates to an edge height change of one free space wavelength across just several nano-meters. Light propagating in the vertical direction nearly parallel to these edges may still be affected by them. A slight taper of these edges may introduce further effects. In addition, interactions between the phase-shifter and chrome edges may degrade image signal quality. Furthermore, the edge shape may affect optical signals significantly.

In this study, edge effects of chromeless phase-shifting masks were examined for both polarizations for a 5X system at i-line ($\lambda = 0.365\mu\text{m}$, $\text{NA}=0.42$, $\sigma = 0.5$). The masks were glass substrates with alternating 0° and 180° phase-shifting sections of $1.0 \lambda/\text{NA}$. The edge slopes of the three structures studied were 90° , 60° , and 45° with the mid-point of the phase-shifter fixed. These structures were similar to those studied by Doi, but with larger periods typically used in manufacturing. The resulting images for edge slopes of 90° and 45° are plotted in Figure 6.8 for both polarizations. All the images were almost identical. The images showed very slight dependence on the edge slope (from 90° to 45°) and almost no polarization dependence.

To further examine variations with respect to phase-shifter geometries, phase-shifting masks were simulated with the same edge slopes but with the base-point of the phase-shifter fixed. Simulated images in Figure 6.9 showed that there was still virtually no polarization dependence. However, the images showed moderate dependence on the edge slopes. Neither the peak intensity nor the linewidth was identical for the phase-shifting and non-phase-shifting sections. Thus area effects rather than edge effects are more important in chromeless phase-shifting masks.

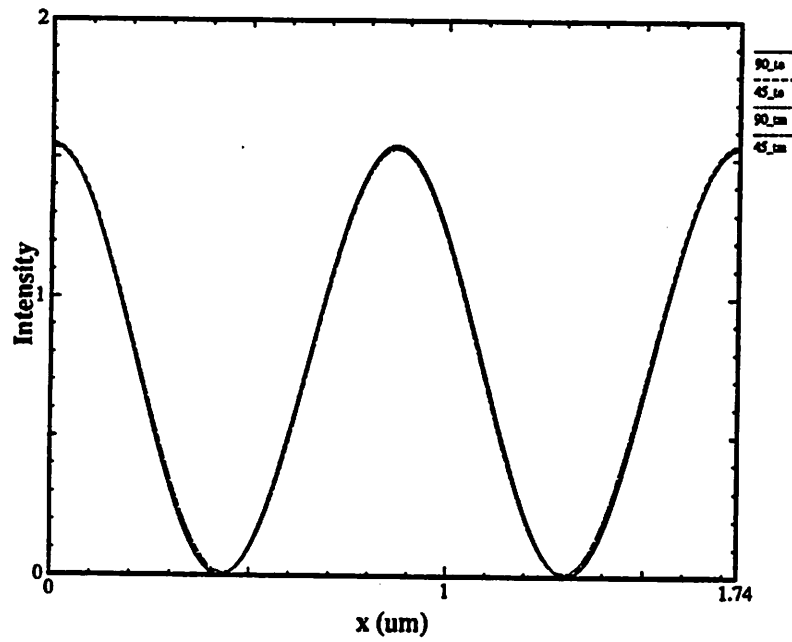


Figure 6.8 Simulated images of chromeless phase-shifting masks. The curves are for both polarizations with edge slopes of 90° and 45° . Neither polarization nor edge effects is important.

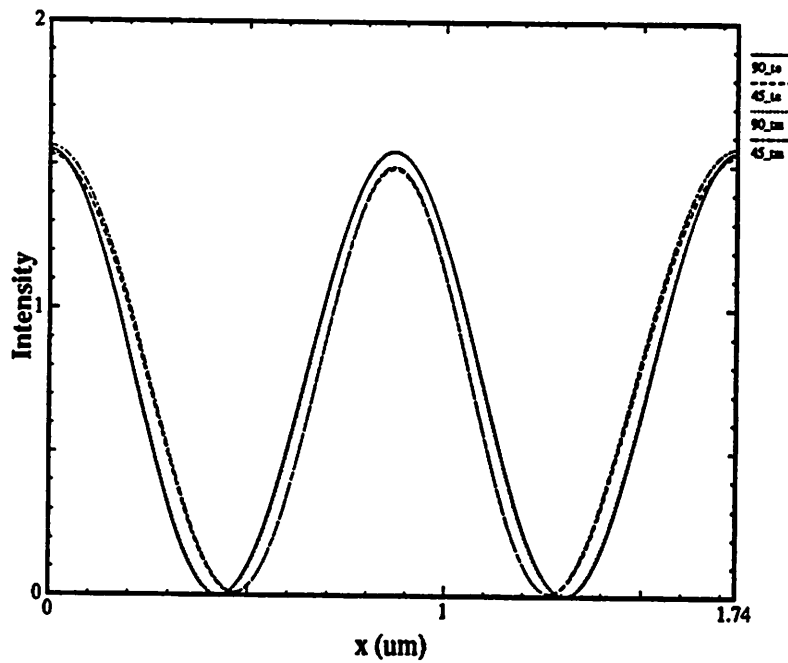


Figure 6.9 Images of chromeless phase-shifting mask with base-point fixed. The images show moderate edge slope dependence, but no polarization dependence.

Besides the ability of phase-shifting masks to print properly, the feasibility of removing defects by double phase-shifting unwanted 180° sections is another concern. In this study, 0° - 360° transitions of four different 360° widths (1.0 , 0.5 , 0.23 , and $0.1 \lambda/\text{NA}$) were simulated. The resulting images for the TE polarization are shown in Figure 6.10. The behavior of the TM polarization is similar. As the width of the 360° phase-shifting section narrowed, the intensity of the 360° region dropped. For the TE polarization, a defect of size $0.5 \lambda/\text{NA}$ decreased the intensity at the 360° region to 81% of the incident intensity. For a defect of size of $0.1 \lambda/\text{NA}$, the intensity at the 360° region dropped to 67% of the incident intensity. For the TM polarization, a $0.5 \lambda/\text{NA}$ defect reduced the intensity to 80% of the clear field intensity whereas a $0.1 \lambda/\text{NA}$ defect caused a drop of intensity to 71%. The decrease in intensity at these double phase-shifted defects may cause undesired printing and is an important area for further characterization.

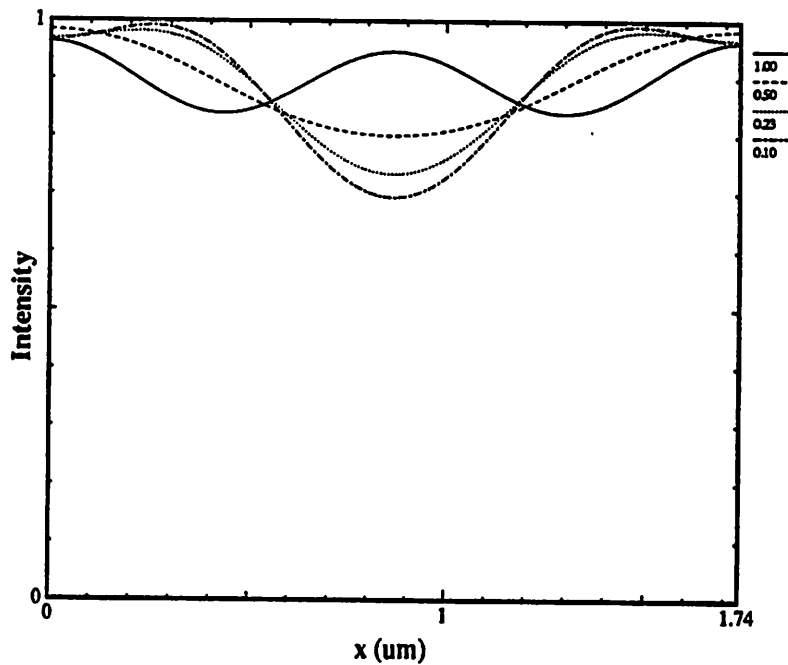


Figure 6.10 Simulated images of 0° - 360° transitions of various sizes for the TE polarization. The intensity drop can be as much as 70% of the clear field value.

6.7 Reflective Masks

The use of a reflective mask integrated into the lens system has been proposed as a means of increasing the field of view in the half-field Dyson approach¹⁵. The basic reflective mask is similar to an overcoated mask. Transmitted light is absorbed in the overcoating absorber layer and light reflected from the chrome is used. The possibility of built-in phase-shifting associated with reflection from material with a smaller refractive index may enhance resolution. In this study, four reflective masks with different chrome edge slopes and absorber materials were simulated: (a) the first mask had vertical edges and was coated with a baked resist like material of refractive index (1.7, 0.1), (b) the second mask had the same coating material but the edge had a slope of 45°, (c) the third mask had a chrome edge slope of 45° and was coated with a PMMA like material of refractive index (1.3, 0.1), and (d) the last mask had a chrome edge slope of 45° and was not coated. All the masks had a 1.0 μm period with a chrome opening of 0.25 μm .

For absorber material with refractive index (1.7, 0.0), there is no built-in phase-shifting associated with reflection from the absorber. Reflective images from the masks for a 1X deep-UV system ($\lambda = 0.248\mu\text{m}$, $\text{NA}=0.7$, $\sigma = 0.5$) are shown in Figure 6.11 for both polarizations for masks (a) and (b). The TE mode shows a steeper image slope as well as more ringing at the chrome edges than the TM polarization. The edge slope of the chrome has almost no effect on the image, except for smoothing the ringing slightly. For reflective masks with built-in phase-shifting, improvements in image slopes were observed for both polarizations. The TE polarization again showed a slightly steeper image slope but more ringing at the chrome edge. Images associated with masks (c) and (d) are shown in Figure 6.12. Built-in phase-shifting also increased the amount of ringing at the chrome edges as well as the intensity in the dark region. In general, the TM polarization is better behaved than the TE polarization for the reflective mask technology in the sense that the TM mode shows less ringing in the image.

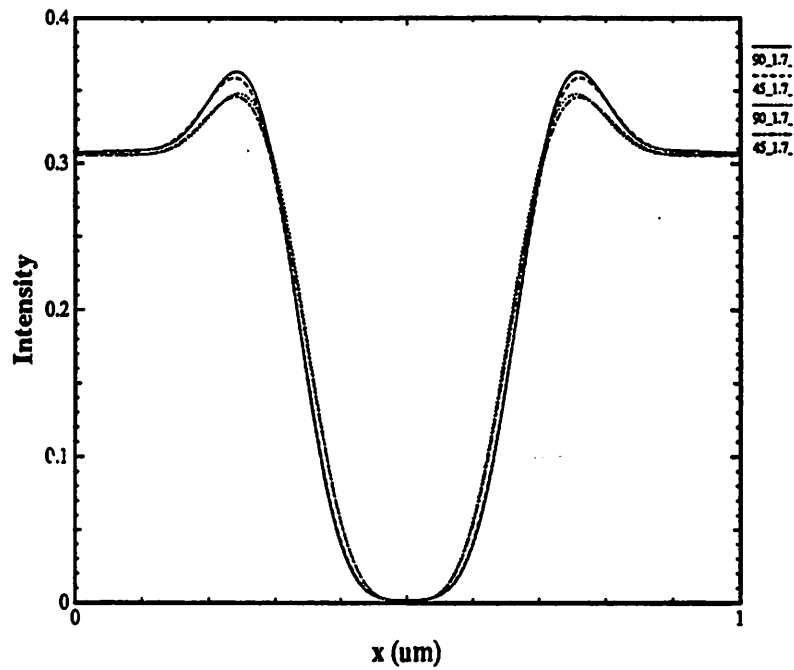


Figure 6.11 Images for reflective masks with no built-in phase-shifting. There is very little edge effects, and the TE mode shows more ringing at the chrome edges

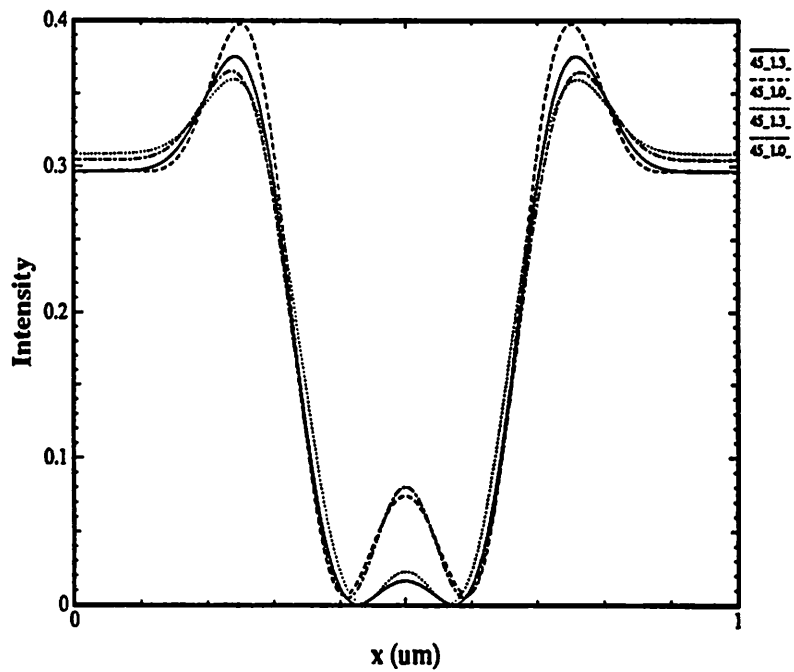


Figure 6.12 Images for reflective masks with built-in phase-shifting. The images show slightly steeper image slopes but more ringing than those in Figure 6.11.

6.8 Conclusion

The importance of polarization effects in mask technologies for scaling optical projection printing was assessed using simulations. The analysis was carried out by using extensions to the massively parallel time-domain TEMPEST program for TM polarization and for outgoing boundary condition in dielectric materials. Historically, the TM polarization has been more troublesome, for example, in the analysis of diffraction gratings. However, for mask technologies, the TM polarization generally shows less edge effects than the TE polarization. Transmission is higher for the TM polarization as well. The use of outgoing boundary condition cleared up confounding mask top surface reflection effects. It appears that mask overcoating can improve transmitted intensity primarily through reduction in reflection upon exiting through the open areas of the mask. Phase-shifting masks studies show little polarization dependence in tapers on chromeless masks. To repair a defect on a phase-shifting mask by double phase-shifting may cause undesired printing as the intensity drops to as much as 70% of the clear field intensity for a $0.1 \lambda/\text{NA}$ defect. Finally, for the reflective mask technology, the use of built-in phase-shifting absorber materials improves the image slope, and the TM polarization shows less ringing than the TE polarization.

Chapter 7

Conclusions and Future Work

The time-domain finite-difference algorithm of TEMPEST was shown to be useful in solving electromagnetic problems. Extension of the program to the TM polarization changes only the multiplicative coefficients but not the form of the updating equations. Oblique incident problems are simplified with the assumptions of periodic structures and zero phase difference between the east and west boundaries. With the left-right periodic boundary condition, only slight modifications in the algorithm are necessary. Image synthesis based on Hopkins' approach allows modeling of realistic projection systems in photolithography.

Extension of TEMPEST for closer integration with other computer simulation and design tools such as SAMPLE¹⁸ and SIMPL¹⁹ within the TCAD framework is worthwhile. Integration with other programs can better model the integrated circuit fabrication process, for instance, by generating simulation structures using SIMPL instead of creating idealized simulation geometries.

Another useful extension to the current program is the analysis of partial coherence effects. Analysis of partial coherent effects is especially important with high NA systems as constant diffraction efficiency with respect to illumination angle is no longer a good assumption. A possible approach to this problem is to simulate a structure with TEMPEST for various illumination angles and then superpose the simulation results. Another possible approach is to insert a phase which is a function of the partial coherence factor σ in the analytically calculated excitation function.

Experience with TEMPEST simulations shows that numerical instability occurs for highly dispersive materials. This is true whenever a material has an imaginary refractive index larger than the real part. The negative value of permittivity thus results causes the field components to diverge. A possible method to remedy this problem is through the use of the convolution relation between the electric displacement \vec{D} and the electric field \vec{E} ²⁰.

Although the current program is efficient and accurate, TEMPEST is limited by its inability to solve three-dimensional problems such as a contact hole. An obvious extension of the program is therefore three-dimensional analysis. With the current available resources, three-dimensional problems that TEMPEST can solve are limited due to the inadequate number of processors. For example, based on accuracy considerations⁸, at least 256 simulation nodes are necessary for 1.0 μm of chrome at a wavelength of 248 nm. Therefore, a 4.0 μm by 4.0 μm by 2.0 μm three-dimensional domain containing silicon requires at least 2^{23} simulation nodes. Even with the largest CM currently available with 32k physical processors and a virtual processor ratio of 64, the maximum number of simulation nodes for a particular problem is 2^{21} , 4 times below the required number of 2^{23} . Therefore, with the current resources, three-dimensional simulation on TEMPEST can only be done on relatively small structures or geometries with a high wavelength to period ratio or on structures containing materials with low refractive index. However, with larger and more powerful parallel computer architectures in sight in the future or with new algorithmic approaches, parallel computers may be an effective tool in solving electromagnetic problems.

References

- 1 Roberto Guerrieri, Karim H. Tadros, John Gamelin, and Andrew Neureuther, "Massively Parallel Algorithms for Scattering in Optical Lithography," *IEEE Trans. on CAD*, vol. 10, no. 9, pp. 1091-1100, Sep. 1991.
- 2 K. S. Yee, "Numerical Solution of Initial Boundary Value Problems Involving Maxwell's Equations in Isotropic Media," *IEEE Trans. Ant. Prop.*, vol. 14, pp. 302-307, May 1966.
- 3 G. Wojcik, D. Vaughn, and L. Galbriath, "Calculation of Light Scatter from Structures on Silicon Surfaces," *Proc. SPIE, Optical/Laser Microlithography*, vol. 772, pp. 21-31, 1987.
- 4 K. Tadros, A. R. Neureuther, J. Gamelin, and R. Guerrieri, "Investigation of Reflective Notching with Massively Parallel Simulation," *Proc. SPIE, Optical/Laser Microlithography III*, vol. 1264, pp. 322-332, Mar. 1990.
- 5 K. Tadros, A. R. Neureuther, and R. Guerrieri, "Understanding Metrology of Polysilicon Gates through Reflectance Measurements and Simulation," *Proc. SPIE, Integrated Circuit Metrology, Inspection and Process Control V*, vol. 1464, Mar. 1991.
- 6 T. Doi, K. Tadros, B. Kuyel, and A. R. Neureuther, "Edge-profile, Materials and Protective Coating Effects on Image Quality," *Proc. SPIE, Integrated Circuit Metrology, Inspection and Process Control V*, vol. 1464, Mar. 1991.
- 7 A. Wong, T. Doi, D. Dunn, and A. R. Neureuther, "Experimental and Simulation Studies of Alignment Marks," *Proc. SPIE, Optical/Laser Microlithography IV*, vol. 1463, Mar. 1991.

- 8 John Gamelin, "Simulation of Topography Scattering for Optical Lithography with the Connection Machine," *M. S. Thesis*, Memorandum No. UCB/ERL M89/71, University of California, Berkeley, May 1989.
- 9 Gerrit Mur, "Absorbing Boundary Conditions for the Finite-Difference Approximation of the Time-Domain Electromagnetic-Field Equations," *IEEE Trans. on Electromagnetic Comp.*, vol. EMC-23, no. 4, pp. 377-382, Nov., 1981.
- 10 Bjorn Engquist, and Andrew Majda, "Radiation Boundary Conditions for Acoustic and Elastic Wave Calculations," *Comm. on Pure and Applied Math.*, vol. 32, pp. 313-357, 1979.
- 11 Born & Wolf, *Principles of Optics*, p. 513, Pergamon Press, 1975.
- 12 Lo & Lee, *Antenna Handbook*, p. 5-14, Van Nostrand Reinhold Company, 1988.
- 13 B. Kuyel, AT&T Bell Laboratory, Private Communication, Jul. 1990.
- 14 Al Wagner, IBM, Private Communication, Nov. 1991.
- 15 Dave Markle, Half-Field Dyson System, Private Communication, Dec. 1989, and R. Hsieh et al., Oct. 1990.
- 16 Kenny Toh, "Two-Dimensional Images with Effects of Lens Aberrations in Optical Lithography," *M. S. Thesis*, Memorandum No. UCB/ERL M88/30, University of California, Berkeley, May 1988.
- 17 Michael Yeung, University of California, Berkeley, Private Communication, Feb. 1992.
- 18 W. G. Oldham, S. N. Nandgaonkar, A. R. Neureuther, and M. M. O'Toole, "A General Simulator for VLSI Lithography and Etching Processes: Part I - Application to Projection Lithography," *IEEE Trans. on Electron Devices*, vol. ED-26, no. 4, pp. 717-722, Apr. 1979.

- 19 M. A. Grimm, K. Lee, and A. R. Neureuther, "SIMPL-1 (SIMulated Profiles from the Layout - Version 1)," *IEDM Technical Digest*, pp. 255-258, 1983.
- 20 C. F. Lee, R. T. Shin, and J. A. Kong, "Finite Difference Method for Electromagnetic Scattering Problems," *Progress in Electromagnetics Research*, Elsevier Press, pp. 415-435, 1991.